Nuclear Engineering and Technology 53 (2021) 618–625

Contents lists available at ScienceDirect

Nuclear Engineering and Technology

journal homepage: www.elsevier.com/locate/net

Original Article

Effect of electric field on primary dark pulses in SPADs for advanced radiation detection applications

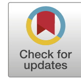

Kyung Taek Lim [a], Hyoungtaek Kim [b], Jinhwan Kim [a], Gyuseong Cho [a,*]

[a] Department of Nuclear & Quantum Engineering, Korea Advanced Institute of Science and Technology, 291 Daehak-ro, Daejeon, 34141, Republic of Korea
[b] Korea Atomic Energy Research Institute, 989, Daeduk-ro, Daejeon 34057, Republic of Korea

ARTICLE INFO

Article history:
Received 9 March 2020
Received in revised form
15 June 2020
Accepted 8 July 2020
Available online 21 July 2020

Keywords:
SPAD
Primary dark pulse
SRH generation
Radiation detection
Field-enhanced
DCR

ABSTRACT

In this paper, the single-photon avalanche diodes (SPADs) featuring three different p-well implantation doses ($\varnothing_{p-well}$) of 5.0×10^{12}, 4.0×10^{12}, and 3.0×10^{12} atoms/cm^2 under the identical device layouts were fabricated and characterized to evaluate the effects of field enhanced mechanisms on primary dark pulses due to the maximum electric field. From the I–V curves, the breakdown voltages were found as 23.2 V, 40.5 V, and 63.1 V with decreasing $\varnothing_{p-well}$, respectively. By measuring DCRs as a function of temperature, we found a reduction of approximately 8% in the maximum electric field lead to a nearly 72% decrease in the DCR at $V_{ex} = 5$ V and T = 25 °C. Also, the activation energy increased from 0.43 eV to 0.50 eV, as decreasing the maximum electric field. Finally, we discuss the importance of electric field engineering in reducing the field-enhanced mechanisms contributing to the DCR in SPADs and the benefits on the SPADs related to different types of radiation detection applications.
© 2020 Korean Nuclear Society, Published by Elsevier Korea LLC. This is an open access article under the CC BY-NC-ND license (http://creativecommons.org/licenses/by-nc-nd/4.0/).

1. Introduction

A single-photon avalanche diode (SPAD), or also known as a Geiger-mode avalanche diode, is a solid-state photodetector that is composed of a reverse-biased p/n junction diode connected in series to a quenching resistor. In comparison to typical avalanche photodiodes, an SPAD operates in a limited Geiger–Müller mode in which an avalanche multiplication process generates large electrical output signals comparable to that of the traditional photomultiplier tube (PMT). Due to a high internal gain, an SPAD is capable of detecting weak light intensities down to a single-photon level [1]. Also, detecting a higher photon intensity is achievable by configuring multiple SPADs in parallel to a common silicon substrate, i.e., a silicon photomultiplier (SiPM), so that its output pulse is proportional to a chronological superposition of current pulses from fired SPADs [1]. Therefore, many works related to SPADs are often reported as a part of SiPM technology [2,3,25,37].

Due to a significant enhancement on the semiconductor process over past decades, performances of unit SPAD have grown remarkably and, as a result, SPADs emerged as a well-established solid-state detector that has garnered tremendous interest in industrial and research fields, such as nuclear medicine, radiation protection, high-energy physics, and remote-sensing technology [4–9]. In particular, arrays of SPADs have been considered a promising candidate to replace traditional PMTs in many radiation detection applications owing to their numerous advantages over PMTs, such as compactness, fast time response, high detection efficiency, low operational voltage, and insensitivity to magnetic fields [10]. Depending on a target application, however, one of the major sources limiting the performance of SPADs is the dark noise. For example, large sensitive areas are often required for detecting cosmic rays, e.g., the Cherenkov Telescope Array, and this can put strict constraints on the maximum dark noise allowed in SPADs for practical usage [11].

The dark noise in a SPAD refers to the number of current pulses developed in the absence of light, which are indistinguishable from signals generated via optical interactions. The noise sources include the primary events, i.e., dark count rate (DCR) and correlated events such as after-pulsing [12]. In particular, three main sources that contribute to the DCRs in SPADs are known as a combination of the diffusion of carriers, the thermal generation of carriers through the Shockley–Read–Hall (SRH) process, and the band-to-band tunneling processes [12]. Although the three mechanisms may coexist, the relative importance of each mechanism depends on an operating temperature because they feature different dependence

* Corresponding author.
E-mail address: gscho@kaist.ac.kr (G. Cho).

https://doi.org/10.1016/j.net.2020.07.006
1738-5733/© 2020 Korean Nuclear Society, Published by Elsevier Korea LLC. This is an open access article under the CC BY-NC-ND license (http://creativecommons.org/licenses/by-nc-nd/4.0/).

on temperature in silicon [13,14]. Nevertheless, given that a typical SPAD structure operates near the room temperature regime, the primary mechanism contributing to DCRs can be considered as the SRH generation process through deep-level defects present in a depletion region (e.g., epitaxial-layer) [15,32]. More importantly, the SRH generation is considerably influenced by the maximum electric field developed across an avalanche region. That is, the high-field can act on deep levels (e.g., metallic impurities) and ultimately induce an increase in the DCR through the field-enhanced mechanisms such as the Poole-Frenkel effect and phonon-assisted tunneling [15,16]. To understand the physics behind the DCR in SPADs, numerous modeling and simulation studies have been performed [17–19]. Also, the progress in the previous studies has led other researchers to establish analytical modeling of high electric fields in avalanche breakdown to explain the field-enhanced mechanisms contributing to DCRs [20–22].

In this paper, we investigate how quantitative changes in the peak electric field can influence the dark noise in SPADs. Therefore, SPADs with three different maximum electric fields were designed and fabricated. For each sample, we start with the temperature dependence on a breakdown voltage (V_{BD}) to emphasize the importance of adjusting the bias voltage to the ambient temperature. Then, we measure DCRs as a function of photon detection efficiency (PDE) to identify the presence of field-enhanced mechanisms in fabricated SPADs. Finally, we measure DCRs as a function of temperature and extract the activation energy for each device, which serves as an indicator of a dominant mechanism contributing to the DCR, to demonstrate the degree to which the field-enhanced mechanisms can influence the DCRs concerning the different maximum electric fields. Furthermore, we discuss some of the benefits of electric field engineering on SPADs related to different types of radiation detection applications.

2. Materials and methods

2.1. Device fabrication

The devices presented in this work are based on an n-on-p structure that was fabricated previously at the National Nanofab Center (NNFC), as depicted in Fig. 1 [23]. The substrate is an 8″ p-type epitaxial wafer with a resistance of 4.0 Ω-cm and a thickness of 4.5 μm. Also, the microcell pitch is 65 μm with a fill factor of 67%. Maintaining the wafer specifications, fabrication conditions, and the device layout identical to the previous version, three different boron implantation doses were applied to the p-well formation to attain SPADs with different electric field profiles. After each p-well implantation, we applied for 165 min a thermal annealing of 1000 °C, which is one of the major processes that cures the defect sites generated from the ion implantation. Fig. 2 shows calculated electric field distributions at V_{BD} of each p-well implantation dose ($\varnothing_{p-well}$) via 2D Silvaco TCAD: for $\varnothing_{p-well}$ of 5.0×10^{12}, 4.0×10^{12}, and 3.0×10^{12} atoms/cm^2, their expected peak electric fields correspond to 5.95×10^5, 5.78×10^5, and 5.46×10^5 V/cm, respectively. Because it was challenging to target for an exact value on the peak electric field, the values of the $\varnothing_{p-well}$ were chosen instead so that the peak values would lie roughly between 5.0×10^5 and 6.0×10^5 V/cm based on the TCAD simulation. As expected, we see that the peak electric fields at the metallurgical junction decreased with a decreasing $\varnothing_{p-well}$ because the magnitude of the peak electric field is determined by integrating the doping profile in the depletion region at a given bias voltage. Also, as $\varnothing_{p-well}$ decreased, the electric field in the depletion region beyond 0.5 μm is extended, and this increase is due to the fact that the doping profile becomes more dispersed with a smaller $\varnothing_{p-well}$. To make the terminology straightforward, we will hereafter refer to the SPADs with $\varnothing_{p-well}$ of 5.0×10^{12}, 4.0×10^{12}, and 3.0×10^{12} atoms/cm^2 as device #1, device #2, and device #3, respectively (Table 1).

2.2. Sample selection and experiment setup

Due to the statistical variations during the fabrication process, and the quality of the starting substrate, the current to voltage (I–V) characteristics of SPADs were not entirely uniform throughout the entire wafer. Thus, prior to the device packaging, wafer-level I–V

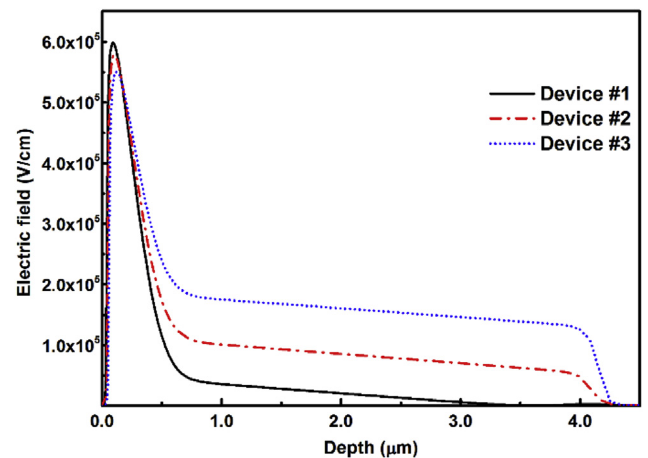

Fig. 2. Simulated electric field distribution of SPADs with three $\varnothing_{p-well}$ conditions at the breakdown voltage.

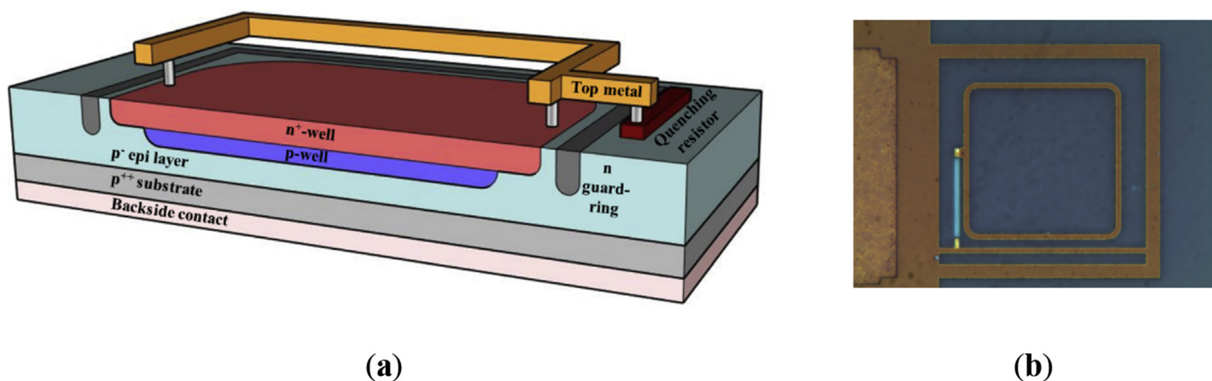

Fig. 1. (a) Diagram of the n-on-p SPAD. (b) Micrograph of the SPAD with a size of 65 μm.

Table 1
Applied $\varnothing_{p-well}$ conditions and their corresponding simulated peak electric field strengths.

Samples	P-well implantation dose, $\varnothing_{p-well}$(atoms/cm^2)	Simulated peak electric field @ V_{BD} (V/cm)
Device #1	5.0×10^{12}	5.95×10^5
Device #2	4.0×10^{12}	5.78×10^5
Device #3	3.0×10^{12}	5.46×10^5

measurements were carried out using a SUMMIT 11742B semi-auto probe station with an Agilent 4284A LCR meter and a 4156C parameter analyzer to select the sample that would represent each family [23]. Fig. 3 (a) shows an example of a fabricated wafer with 64 reticles. Based on the previously reported I–V measurements for each wafer [23], we acquired 2D mapping of reference voltages (e.g., the voltage at the maximum slope) and corresponding currents at 1 V above the reference voltages for all samples. Then, we calculated the mean and standard deviation of the reference voltages to find the sample that had values close to their average, e.g., they were measured as 23.58 ± 0.87 V, 40.84 ± 1.08 V, 63.52 ± 0.93 V for device #1, device #2, and device #3, respectively. The selected samples were then packaged on ceramics for further analysis.

Fig. 3 (b) presents the general setup used for the V_{BD}, DCR, and photon detection efficiency (PDE) measurements carried out for packaged samples. To investigate the temperature dependence on fabricated devices, the sample was mounted on the CAEN SP5650 sensor holder that was attached to the CAEN SP5600 amplifier via extension cables and placed inside the JEIO TECH PBV025 temperature chamber. Then, the output of the amplifier was connected to a PC through a CAEN DT5720A digitizer to acquire the pulse histogram. At each temperature, the chamber was sealed tightly and left for enough time to ensure a stable ambient temperature was achieved. Also, the temperature on the detector was measured directly through a built-in temperature module in the SP5600. For PDE measurements, an IS235A integrating sphere along with the Monora200 monochromator with a wavelength of 560 nm was applied to make a uniform light source, and Thorlabs PM100 was used as a reference diode for the photon flux calibration.

3. Results and discussions

3.1. Reverse current-voltage curves

We can gain some useful insights regarding the device properties by looking at the I–V curves near the breakdown region in SPADs belonging to three $\varnothing_{p-well}$ conditions (Fig. 4). From the I–V curves, the voltage at which the avalanche breakdown is expected to occur for each device is found as 23.2 V, 40.5 V, and 63.1 V for device #1, device #2, and device #3, respectively. Having the avalanche breakdown as the base point, the reverse current of an SPAD can be divided into two regions, i.e., the pre-breakdown and post-breakdown regions. The pre-breakdown current, which is mainly caused by a surface and peripheral leakage current, is similar for all three samples near ten pA [24]. In the post-breakdown region, on the other hand, the three devices exhibit different current levels: going from device #1 to device #3, the current level decreases, as shown in Fig. 4 (b). The post-breakdown current depends on the carriers that contribute to the avalanche multiplication process inside the depletion region, i.e., the bulk current [24]. This suggests that the lower current level in the post-breakdown region could be partially due to the reduced primary dark pulses from the weakened influence of the field-enhanced mechanisms. It should be noted, however, that other factors also contribute to the decrease in the post-breakdown region with decreasing $\varnothing_{p-well}$, such as a multiplication gain, after-pulsing, and avalanche triggering probability [25]. For example, it was shown that the gain of an SPAD decreases with decreasing $\varnothing_{p-well}$ at a fixed applied voltage [23].

3.2. Breakdown voltage

A bias point at which the derivative of log (I) had its maximum is considered as V_{BD} [26]. However, it is challenging to apply I–V measurements in a condition where V_{BD} changes with temperature. Therefore, we used the V_{BD} as a bias point at which the avalanche pulses start to arise on an oscilloscope as increasing a bias voltage. Fig. 5 shows the V_{BD} as a function of temperature for the three devices. As expected, the breakdown voltage increased with the increasing temperature in all three samples. The reason is that there is a minimum requirement for the electric field to initiate an impact ionization successfully, and such condition depends on

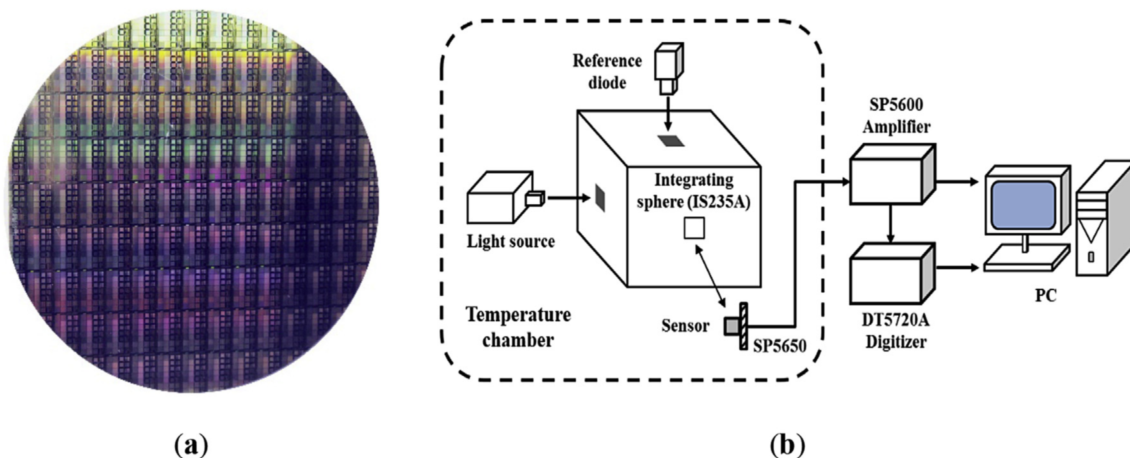

Fig. 3. (**a**) Example of the fabricated 200 mm wafer with 64 reticles. (**b**) Block diagram of the experimental setup used for the device characterization.

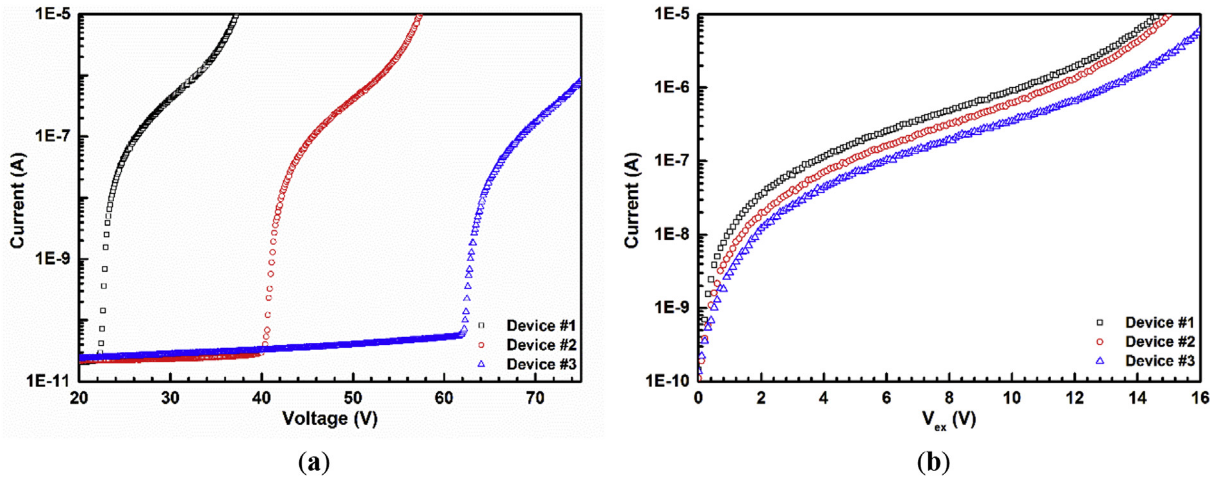

Fig. 4. (**a**) Reverse current as a function of voltage near the breakdown region for three $\varnothing_{p-well}$ conditions. (**b**) Reverse current as a function of excess voltage in the post-breakdown region for direct comparison.

the mean free path for phonon scattering and the ionization threshold energy [27]. In particular, the mean free path for phonon scattering decreases with increasing temperature [28]. Thus, the generated carriers require a higher bias voltage to gain sufficient energy to initiate the avalanche multiplication process, e.g., an increase in V_{BD}.

Furthermore, the temperature coefficients of V_{BD} (T_{coeff}) were found to be 53.6 mV/°C, 72.8 mV/°C, and 86.9 mV/°C for devices #1, #2, and #3, respectively. Indeed, the magnitude of T_{coeff} increases as the $\varnothing_{p-well}$ decreases, i.e., the rate at which the V_{BD} changes with respect to the temperature is greater when the maximum electric field is lower at the p/n junction. The main reason for the various T_{coeff} is attributed to the different depleted width and electric field profiles among the three samples. Because the depletion depths of devices #2 and #3 are broader than that of device #1, as shown in Fig. 2, the electric field profiles are more dispersed in two devices. As a result, the additional voltage required to initiate the same avalanche breakdown after an increment of temperature is larger in the wider region [28]. Therefore, the shift in V_{BD} resulting from temperature fluctuation is smaller as $\varnothing_{p-well}$ increases due to a more locally-confined electric field within a narrower depletion width [28]. Having a smaller temperature dependence for V_{BD} can be beneficial in applications that require a long-time data acquisition. For example, in a PET system where a fixed bias voltage is applied, a minimal shift in the photopeak due to the temperature variation with time would be favorable in improving the spatial resolution and in reducing the complexity of PET scanner calibration [29]. In the following analysis, V_{bias} was adjusted as to the temperature to ensure that V_{ex} would remain constant throughout all of the DCR measurements and to eliminate the V_{BD}–temperature dependency.

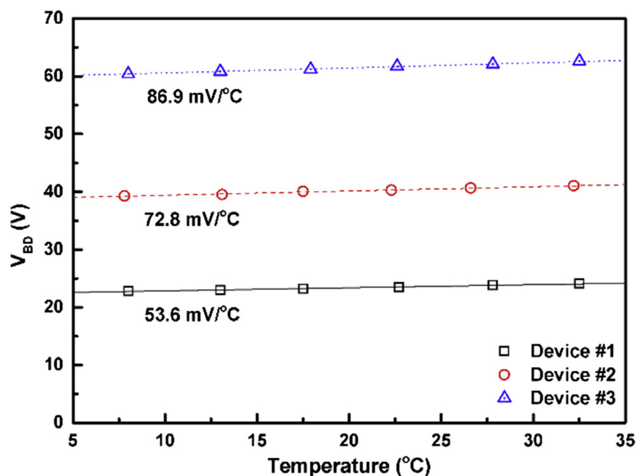

Fig. 5. The V_{BD} as a function of temperature in devices with three $\varnothing_{p-well}$ conditions.

3.3. Dark count rate

For SPADs operating at near room temperature, the dominant process that contributes to dark noise is considered as the SRH generation of carriers. As mentioned previously, other noise sources, such as diffusion of carriers and band-to-band tunneling, can also influence dark noise in SPADs. Nevertheless, it has been reported that the degree to which two mechanisms mentioned above contribute to dark noise becomes significant at a temperature above or below the room temperature regime [30]. Thus, in this paper, we focus on the dominant mechanism that contributes to the DCR in SPADs operating at room temperature regime, i.e., thermal generation of carriers due to SRH statistics.

In general, the primary noise due to SRH generation depends on the levels of structural defects and metal contaminations, so the higher the defect concentration is, the lower the effective lifetime would be, and thus, the higher the rate of pulses generated in the dark condition [14]. Given that the magnitude of the maximum electric field is less than 10^5 V/cm (e.g., low-field), the generation rate of SRH process in depleted p/n junction silicon is approximately equal to [30].

$$U_{SRH} \approx \frac{N_t \sigma \upsilon_{th} n_i}{2\cosh\left(\frac{E_0 - E_t}{k_B T}\right)} = \frac{n_i}{\tau_{g,0}}, \tag{1}$$

Where U_{SRH} is the generation rate due to the pure SRH process, n_i is the intrinsic carrier concentration, N_t is the concentration of defect sites or traps, σ is the e^- or h^+ capture cross-section of the trap, υ_{th} is the thermal velocity of e^- or h^+, k_B is the Boltzmann constant, T is the temperature in Kelvin, E_0 is the intrinsic Fermi level, E_t is the trap energy, and $\tau_{g,0}$ is the generation lifetime of minority carriers. From the equation above, it can be noted that $\tau_{g,0}$ is determined by the *cosh* of the difference between the E_t and E_0, i.e., only the traps

with energy very close to the intrinsic energy level have a considerable influence to the generation of carriers in the depletion region.

Aside from the epitaxial-layer quality, the presence of a high electric field in the depletion region can cause an increase in the U_{SRH} further by inducing tunneling of trapped carriers via field-enhanced mechanisms [31]. Note that the 'tunneling' due to the field-enhanced mechanism (e.g., indirect tunneling) should not be confused with the band-to-band tunneling (e.g., direct tunneling) as they are two different mechanisms. Under the assumption of a single deep level impurity, the generation rate under the high field-effect can be rewritten as [32]:

$$U_{SRH,eff} = \frac{n_i}{\tau_{g,eff}}, \quad \text{where } \tau_{g,\,eff} = \frac{\tau_{g,0}}{(1+\Gamma)}. \tag{2}$$

Here, $U_{SRH,\,eff}$ is the generation rate due to the field-enhanced SRH generation, $\tau_{g,\,eff}$ is the effective generation lifetime with a high electric field, and Γ is the field-enhancement factor. The factor Γ is strongly dependent on the local electric field strength and on the type of impurity centers and charge states, e.g., acceptor-like and donor-like deep levels [32,33]. The equation above implies that the larger the value Γ due to field-enhanced mechanisms is, the smaller $\tau_{g,\,eff}$ would be; thus, the larger the DCR would be expected in an SPAD. Therefore, they play a significant role in enhancing the $U_{SRH,\,eff}$ in SPADs due to their inherently high internal electric field at the metallurgical junction.

Fig. 6 shows the DCR per unit area of the three devices for V_{ex} measured from 4 V to 7 V. From the plot, we can see that the DCR increases with increasing V_{ex} in each sample. This is because the V_{ex} dependence of the DCR is expected to reflect the behavior of the avalanche triggering probability [24]. Also, it is clear that, as $\varnothing_{p-well}$ decreases, DCR decreases for a fixed V_{ex}. This decrease could be due to a combination of a smaller triggering probability and a weaker influence of field-enhanced mechanisms contributing to the thermal generation rate through the deep-level impurities with decreasing peak electric field in the high-field region [16,21].

It is worth mentioning that the DCR measurements reported in Fig. 6 do not yet provide sufficient information regarding the degree to which the field-enhanced mechanisms affect the primary dark noise in the fabricated SPADs. This is because other sources have considerable impact on the concentration of defects that are responsible for the overall magnitude of the DCR of a SPAD [25]. Some of these sources include the quality of the wafer and various processes that induce a stress on the junction such as ion implantation and high-temperature annealing. In particular, the number of deep-level traps (e.g., transition-metal impurities) introduced during the ion implantation are subject to the implantation dose and energy. In this regard, the degree to which the peak electric field is reduced due to the lower $\varnothing_{p-well}$ may not fully reflect the reduction in the DCR as observed in Fig. 6.

Nevertheless, the influence of field-enhanced SRH on the DCR can be exemplified by measuring the DCR as a function of PDE at its peak wavelength. For instance, given that a green-sensitive SPAD is illuminated by the light of its peak wavelength, the PDE is expected to increase with increasing V_{ex}. This is demonstrated in Fig. 7 where the PDE of fabricated devices are measured as a function of V_{ex} from 4 V to 7 V by illuminating the samples with a monochromator at a wavelength of 560 nm. However, at a certain point, the PDE is expected to be saturated in all devices because the triggering probability cannot exceed the theoretical value of one [34]. Given that the device has a microcell size of 35 μm, the saturation in the PDE with increasing over-voltage is apparent even at a relatively lower V_{ex} and the PDE is almost saturated to 60% at V_{ex} of 10 V [35]. Likewise, a similar situation could be reached for the DCR if the device is in pure SRH condition; however, when the field-enhanced mechanisms are present, DCR would keep increasing with respect to V_{ex} even if the triggering probability reaches its maximum value [35]. This is because generation due to the field-enhanced SRH also depends on the V_{ex} applied to the SPAD [32]. That is, when V_{ex} is increased, the electric field in the depletion region becomes stronger and increases the tunneling probability of carriers captured at the trap centers, hence reducing the carrier lifetime according to Equation (2). In this regard, one may anticipate a non-linear relationship between the DCR and PDE given that the contribution of field-enhanced mechanisms on the SRH generation is considerable.

Fig. 8 shows the plot of the DCR per unit area as a function of PDE at 560 nm measured on samples with three $\varnothing_{p-well}$ conditions. For device #1 and #2, the DCR is nearly proportional to the PDE in the beginning; however, it starts to deviate as the PDE increases and eventually becomes non-linear, especially at relatively high PDE. In other words, while the electron triggering probability (and thus the PDE) on the depletion edge in the p-layer tends to saturate with increasing V_{ex}, the field-enhanced generation of carriers continues to increase with increasing V_{ex}. Similar behaviors have been reported by other studies where a non-linear increase in the

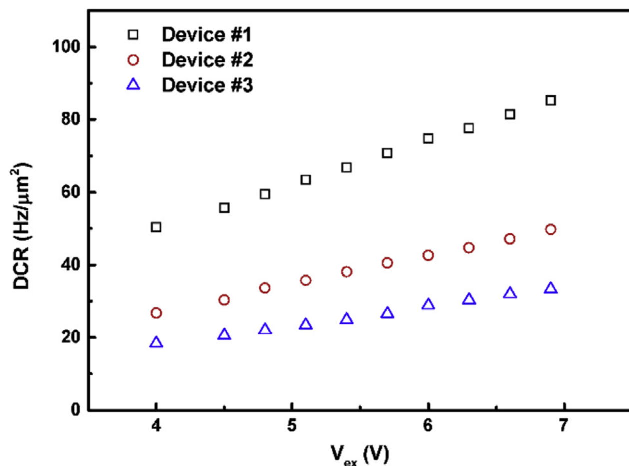

Fig. 6. DCR per unit area of SPADs as a function of V_{ex} in SPADs with three $\varnothing_{p-well}$ conditions.

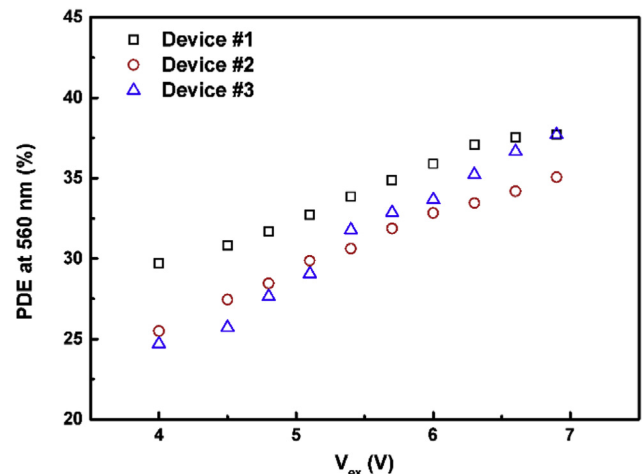

Fig. 7. PDE (at 560 nm) of SPADs with three $\varnothing_{p-well}$ conditions for V_{ex} measured from 4 V to 7 V.

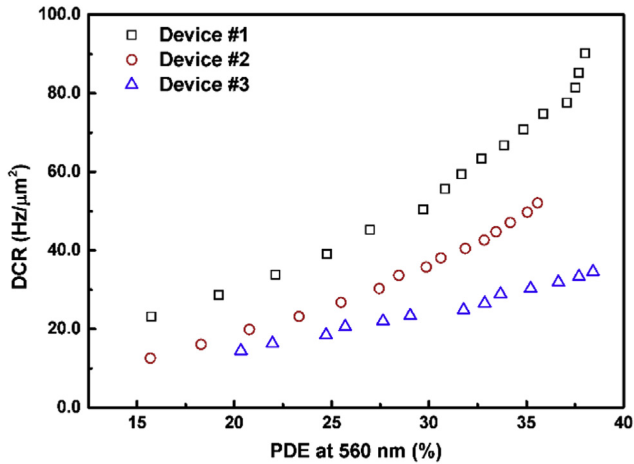

Fig. 8. DCR per unit area as a function of PDE at 560 nm for SPADs with three $\varnothing_{p-well}$ conditions.

DCR is apparent with increasing V_{ex} [35,36]. Note that the expected value of reaching saturation in the PDE at a given wavelength for the fabricated samples is different from those of previous studies due to the different device structure and geometry [37]. Also, it is interesting to point out that we do not quite see this behavior in device #3. This does not suggest that the field-enhanced generation of carriers is non-existing. However, it could possibly be due to a combination of a weakened influence of field-enhanced mechanism over the DCR and a slower growth in the avalanche triggering probability [38] in device #3 in comparison to those of device #1 and #2.

In the following paragraphs, we measure the DCR as a function of temperature to demonstrate the influence of electric fields on the dark noise in SPADs at different temperatures. More importantly, activation energy was estimated from the results to make a better understanding of the influence of the field-enhanced mechanisms for each SPAD in terms of its maximum electric field.

Measurements on DCRs as a function of temperature at $V_{ex} = 5.0$ V are reported in Fig. 9. From the result, we can see that the DCR in all three samples increased with increasing temperature. For example, the DCR in device #1 was around 20 kHz at T = −20 °C, but the value increases exponentially with increasing temperature, reaching the value of about 560 kHz at T = 40 °C. More importantly, we can see that a lower DCR is achieved with a device of a lower maximum electric field; at T = 25 °C, the measured DCR was around 240 kHz, 140 kHz, and 60 kHz for device #1, device #2, and device #3, respectively. That is, about an 8% decrease in the peak electric field from device #1 to device #3 caused a reduction of approximately 72% in the DCR.

To obtain the activation energy, we plot the natural logarithm of the DCR as a function of temperature, namely, the Arrhenius plot. Then, the slope of ln(DCR) versus 1/kT indicates the activation energy of DCR because the DCR dependence on the temperature is expected to follow a similar law as the generation rate in p/n diodes, i.e., [30].

$$U_{SRH}(T) \sim DCR(T) \sim A \times \exp\left(\frac{-E_A}{k_B T}\right), \quad (3)$$

where E_A is the activation energy of the specific generation process, and A is a constant. Hence, the temperature dependency of the DCR indicates the dominant process contributing to the DCR since the activation energy is associated with a specific generation process inside the depletion region [30].

The Arrhenius plots of three devices at $V_{ex} = 5.0$ V (Fig. 10) for the temperature range investigated in Fig. 9 shows that the magnitude of E_A in all three samples. It should be noted that the linear fits were performed for temperatures from 5 °C to 30 °C instead of fitting over the entire measured range. The reasons are as follows. First, the region of interest is in the room temperature regime because, at that temperature, the field-enhanced SRH generation is expected to be the dominant source of primary dark pulses in the high-field region [30,32]. Second, a slight deviation from linear behavior in the lower temperature region (e.g., below zero) suggests that another mechanism, such as band-to-band tunneling, is possibly dominating the generation process [32].

In a case of pure SRH, the value E_A in silicon is expected to be close to $E_g/2$ [14]. However, the extracted values of E_A in Fig. 10 were less than $E_g/2$. What this shows is that all three devices are indeed influenced by the field-enhanced mechanisms; in the presence of a strong electric field, the tunneling of captured carriers at trap centers increases with increasing electric field strength. In turn, this causes an enhanced deviation from pure SRH statistics (e.g., changing the $\tau_{g,\ eff}$) and hence, a reduction of the E_A [30]. In addition, the magnitude of E_A increased from device #1 to device #3, approaching the expected value of pure SRH generation. As seen in

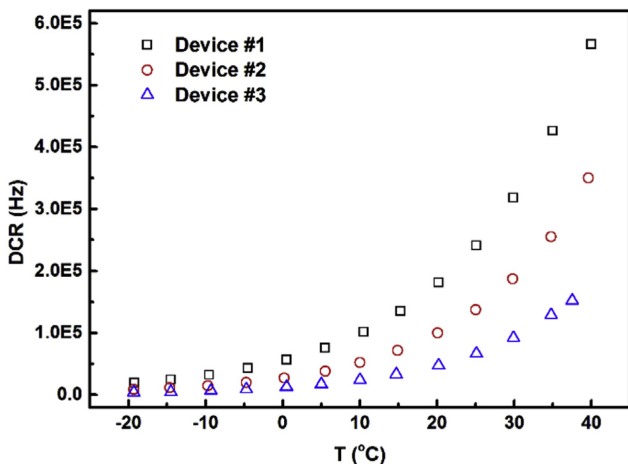

Fig. 9. Dark count rate as a function of temperature for three $\varnothing_{p-well}$ conditions at $V_{ex} = 5.0$ V.

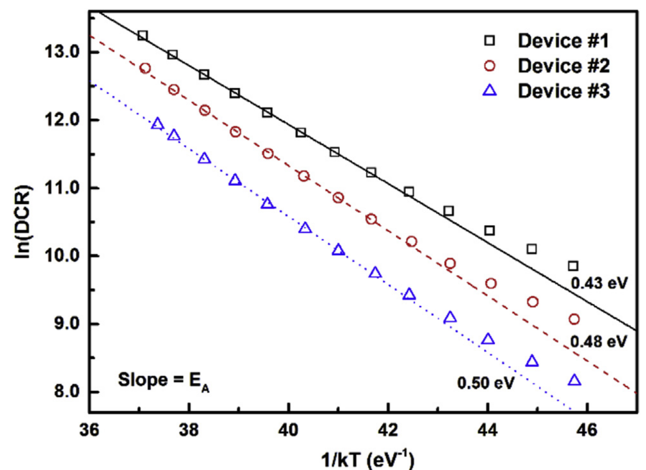

Fig. 10. The Arrhenius plot of three samples at $V_{ex} = 5.0$ V. The DCR activation energy values were 0.43 eV, 0.48 eV, and 0.50 eV for device #1, device #2, and device #3, respectively.

Table 1, device #1, which featured the strongest peak electric field, had an E_A value of 0.43 eV, whereas device #3, which had the weakest peak electric field, had an E_A value of 0.50 eV. The increase in E_A from device #1 to device #3 is indeed due to suppression of the field-enhanced SRH generation as a result of the reduced maximum electric field [35]. That is, the probability of trapped carriers tunneling through the potential barrier is lowered with decreasing field-enhancement factor Γ [32], and hence, less contribution is made to the generation of primary dark pulses due to the reduced weight of the field-enhanced mechanisms. We also observe that all three devices begin to deviate from the fitted curve at low temperatures (e.g., below zero). These deviations from the expected line fits suggest that, for $T < 0$ °C, the field-enhanced SRH generation is no longer the dominant mechanism responsible for the DCR and that the weight of other mechanisms contributing to the DCR is becoming considerable [32].

We should also point out that the E_A for pure SRH process in silicon is not always expected to be 'equal to' $E_g/2$ or 0.56 eV; the E_A in pure SRH generation is commonly close to $E_g/2$, but the exact value depends on the types of impurities present in silicon. The primary effect of field-enhanced mechanisms is to change the pure SRH generation time constant ($\tau_{g,0}$) to the effective time constant ($\tau_{g,eff}$), as reported in Equation (2). Nevertheless, the degree to which $\tau_{g,eff}$ is influenced by the field-enhanced mechanisms is determined by the Γ or the strength of the electric field; a reduced Γ due to a lower electric field would lead to a smaller $\tau_{g,eff}$ and hence results in a less deviation from the pure SRH statistic. Therefore, it clearly shows that the influence of the field-enhanced mechanisms at the generation centers is significant. Furthermore, the degree to which the field-enhanced mechanisms influence the existing DCR strongly depends on the electric field strength at the multiplication region.

4. Conclusion

In this paper, we demonstrated the degree to which the high electric field developed across the multiplication region can influence the DCR in SPADs via field-enhanced mechanisms. In particular, $\varnothing_{p-well}$ of 5.0×10^{12}, 4.0×10^{12}, and 3.0×10^{12} atoms/cm^2 were applied to create SPADs with three different electric field peaks in descending order. With the devices operating at $V_{ex} = 5$ V and $T = 25$ °C, it was observed that an 8% reduction in the peak value from device #1 to device #3 caused a 72% reduction in the DCR. Furthermore, the fact that the E_A of the three devices shifts from 0.50 eV to 0.43 eV clearly suggests that the field-enhanced mechanism is one of main processes that contribute to the overall DCR in SPADs [32,35].

The advantage of reducing the maximum electric field in SPADs may be found for applications that require a low dark noise at cryogenic temperature or a large detection area exposed to a significant amount of background light [39]. On the other hand, some drawbacks in merely reducing the electric field include a reduction in the PDE and an increase in the V_{BD}, which would be undesirable for applications where the most important parameter is the maximum PDE, e.g., PET. In this regard, a single SPAD design is inadequate to meet the needs of diverse radiation detection applications, and thus, the thoughtful design of the electric field profile within the depletion region must be taken into consideration when designing SPADs for a target application.

Declaration of competing interest

The authors declare that they have no known competing financial interests or personal relationships that could have appeared to influence the work reported in this paper.

Acknowledgments

This work was supported by the Institute of Information & Communications Technology Planning & Evaluation (IITP) grant funded by the Korea government (MSIT) (2019-0-00831).

References

[1] D. Renker, E. Lorenz, Advances in solid state photon detectors, J. Instrum. 4 (2009) P04004.
[2] F. Acerbi, A. Ferri, A. Gola, M. Cazzanelli, L. Pavesi, N. Zorzi, C. Piemonte, Characterization of single-photon time resolution: from single SPAD to silicon photomultiplier, IEEE Trans. Nucl. Sci. 61 (2014) 2678–2686.
[3] F. Acerbi, G. Paternoster, A. Gola, N. Zorzi, C. Piemonte, Silicon photomultipliers and single-photon avalanche diodes with enhanced NIR detection efficiency at FBK, Nucl. Instrum. Methods Phys. Res. 912 (2018) 309–314.
[4] P. Buzhan, A. Karakash, Y. Teverovskiy, Silicon Photomultiplier and CsI(Tl) scintillator in application to portable H*(10) dosimeter, Nucl. Instrum. Methods Phys. Res. 912 (2018) 245–247.
[5] G. Erika, Silicon photomultipliers for high energy physics detectors, J. Instrum. 6 (2011) C10003.
[6] S. Gundacker, F. Acerbi, E. Auffray, A. Ferri, A. Gola, M.V. Nemallapudi, G. Paternoster, C. Piemonte, P. Lecoq, State of the art timing in TOF-PET detectors with LuAG, GAGG and L(Y)SO scintillators of various sizes coupled to FBK-SiPMs, J. Instrum. 11 (2016) P08008. P08008.
[7] R. Agishev, A. Comerón, J. Bach, A. Rodriguez, M. Sicard, J. Riu, S. Royo, Lidar with SiPM: some capabilities and limitations in real environment, Optic Laser. Technol. 49 (2013) 86–90.
[8] G. Ambrosi, M. Ambrosio, C. Aramo, E. Bissaldi, A. Boiano, A. Bonavolontà, C. de Lisio, L. Di Venere, E. Fiandrini, N. Giglietto, F. Giordano, M. Ionica, V. Masone, R. Paoletti, V. Postolache, D. Simone, V. Vagelli, M. Valentino, Development of a SiPM based camera for Cherenkov telescope array, Nucl. Part.Phys. Proc. 291–293 (2017) 55–58.
[9] C. Barker, T. Zhu, L. Rolison, S. Kiff, K. Jordan, A. Enqvist, Pulse shape analysis and discrimination for silicon-photomultipliers in helium-4 gas scintillation neutron detector, EPJ Web Conf. 170 (2018), 07002.
[10] D.J. Herbert, V. Saveliev, N. Belcari, N.D. Ascenzo, A.D. Guerra, A. Golovin, First results of scintillator readout with silicon photomultiplier, IEEE Trans. Nucl. Sci. 53 (2006) 389–394.
[11] M. Stipčević, D. Wang, R. Ursin, Characterization of a commercially available large area, high detection efficiency single-photon avalanche diode, J. Lightwave Technol. 31 (2013) 3591–3596.
[12] G. Collazuol, M.G. Bisogni, S. Marcatili, C. Piemonte, A. Del Guerra, Studies of silicon photomultipliers at cryogenic temperatures, Nucl. Instrum. Methods Phys. Res. 628 (2011) 389–392.
[13] R. Pagano, G. Valvo, D. Sanfilippo, S. Libertino, D. Corso, P.G. Fallica, S. Lombardo, Silicon photomultiplier device architecture with dark current improved to the ultimate physical limit, Appl. Phys. Lett. 102 (2013) 183502.
[14] S.M. Sze, K. Ng, Physics of Semiconductor Devices, third ed., John Wiley & Sons, 2007.
[15] R.H. Haitz, Mechanisms contributing to the noise pulse rate of avalanche diodes, J. Appl. Phys. 36 (1965) 3123–3131.
[16] P.A. Martin, B. Streetman, K. Hess, Electric field enhanced emission from non-Coulombic traps in semiconductors, J. Appl. Phys. 52 (1981) 7409–7415.
[17] R. McIntyre, Multiplication noise in uniform avalanche diodes, IEEE Trans. Electron. Dev. 13 (1966) 164–168.
[18] R. Pagano, S. Libertino, D. Corso, S. Lombardo, G. Valvo, D. Sanfilippo, G. Condorelli, M. Mazzillo, A. Piana, B. Carbone, Silicon photomultiplier: technology improvement and performance, J. Sys. Mea. 6 (2013) 124–136.
[19] R. Pagano, S. Libertino, D. Corso, S. Lombardo, G. Valvo, D. Sanfilippo, G. Condorelli, M. Mazzillo, A. Piana, B. Carbone, G. Fallica, Improvement of the diffusive component of dark current in SiPM pixels, Sensordevices (2012) 2012.
[20] S. Cova, A. Lacaita, G. Ripamonti, Trapping phenomena in avalanche photodiodes on nanosecond scale, IEEE Electron. Device Lett. 12 (1991) 685–687.
[21] G.A.M. Hurkx, D.B.M. Klaassen, M.P.G. Knuvers, A new recombination model for device simulation including tunneling, IEEE Trans. Electron. Dev. 39 (1992) 331–338.
[22] W.J. Kindt, H.W.V. Zeijl, Modelling and fabrication of Geiger mode avalanche photodiodes, IEEE Trans. Nucl. Sci. 45 (1998) 715–719.
[23] K.T. Lim, H. Kim, M. Kim, Y. Kim, C. Lee, G. Cho, Photon-number resolving capability in SiPMs with electric field variation for radiation detection applications, Radiat. Phys. Chem. 155 (2019) 101–106.
[24] C. Piemonte, R. Battiston, M. Boscardin, G.F.D. Betta, A.D. Guerra, N. Dinu, A. Pozza, N. Zorzi, Characterization of the first prototypes of silicon photomultiplier fabricated at ITC-irst, IEEE Trans. Nucl. Sci. 54 (2007) 236–244.
[25] F. Acerbi, S. Gundacker, Understanding and simulating SiPMs, Nucl. Instrum. Methods Phys. Res. 926 (2019) 16–35.
[26] V. Chmill, E. Garutti, R. Klanner, M. Nitschke, J. Schwandt, Study of the breakdown voltage of SiPMs, Nucl. Instrum. Methods Phys. Res. 845 (2017) 56–59.
[27] C.Y. Chang, S.S. Chiu, L.P. Hsu, Temperature dependence of breakdown voltage

in silicon abrupt p-n junctions, IEEE Trans. Electron. Dev. 18 (1971) 391–393.
[28] N. Serra, G. Giacomini, A. Piazza, C. Piemonte, A. Tarolli, N. Zorzi, Experimental and TCAD study of breakdown voltage temperature behavior in n+/p SiPMs, IEEE Trans. Nucl. Sci. 58 (2011) 1233–1240.
[29] X. Li, C. Lockhart, T.K. Lewellen, R.S. Miyaoka, Study of PET detector performance with varying SiPM parameters and readout schemes, IEEE Trans. Nucl. Sci. 58 (2011) 590–596.
[30] C. Piemonte, A. Gola, Overview on the main parameters and technology of modern Silicon Photomultipliers, Nucl. Instrum. Methods Phys. Res. 926 (2019) 2–15.
[31] M. Ghioni, A. Gulinatti, I. Rech, F. Zappa, S. Cova, Progress in silicon single-photon avalanche diodes, IEEE J. Sel. Top. Quant. Electron. 13 (2007) 852–862.
[32] M. Ghioni, A. Gulinatti, I. Rech, P. Maccagnani, S. Cova, Large-area Low-Jitter Silicon Single Photon Avalanche Diodes, SPIE, 2008.
[33] G.A.M. Hurkx, H.C.d. Graaff, W.J. Kloosterman, M.P.G. Knuvers, A new analytical diode model including tunneling and avalanche breakdown, IEEE Trans. Electron. Dev. 39 (1992) 2090–2098.
[34] A.N. Otte, T. Nguyen, J. Stansbury, Locating the avalanche structure and the origin of breakdown generating charge carriers in silicon photomultipliers by using the bias dependent breakdown probability, Nucl. Instrum. Methods Phys. Res. 916 (2019) 283–289.
[35] A. Gola, F. Acerbi, M. Capasso, M. Marcante, A. Mazzi, G. Paternoster, C. Piemonte, V. Regazzoni, N. Zorzi, NUV-sensitive silicon photomultiplier technologies developed at fondazione bruno kessler, Sensors 19 (2019) 308.
[36] A.N. Otte, D. Garcia, T. Nguyen, D. Purushotham, Characterization of three high efficiency and blue sensitive silicon photomultipliers, Nucl. Instrum. Methods Phys. Res. 846 (2017) 106–125.
[37] G. Zappalà, F. Acerbi, A. Ferri, A. Gola, G. Paternoster, V. Regazzoni, N. Zorzi, C. Piemonte, Study of the photo-detection efficiency of FBK High-Density silicon photomultipliers, J. Instrum. 11 (2016) P11010.
[38] C. Piemonte, F. Acerbi, A. Ferri, A. Gola, G. Paternoster, V. Regazzoni, G. Zappala, N. Zorzi, Performance of NUV-HD silicon photomultiplier technology, IEEE Trans. Electron. Dev. 63 (2016) 1111–1116.
[39] I. Ostrovskiy, F. Retiere, D. Auty, J. Dalmasson, T. Didberidze, R. DeVoe, G. Gratta, L. Huth, L. James, L. Lupin-Jimenez, N. Ohmart, A. Piepke, Characterization of silicon photomultipliers for nEXO, IEEE Trans. Nucl. Sci. 62 (2015) 1825–1836.